

<https://doi.org/10.1038/s44304-025-00105-3>

Does discontinuous Mesoscale Convective System produce stronger precipitation?

Check for updates

Aoqi Zhang^{1,2} & Yilun Chen^{1,2}

Mesoscale Convective Systems (MCSs) dominate global precipitation, yet their discontinuous evolution (merging, splitting, complex) and associated mechanisms remain unclear. Using Himawari-8 and IMERG datasets, we classify MCSs into four primary types (continuous, merging, splitting, complex), accounting for 97.15% of MCS-related precipitation. Discontinuous-type MCSs contribute 68.81% of total precipitation, demonstrating their critical role in freshwater supply, agriculture, and ecosystem stability, while posing greater flood risks to human societies. Spatial analyses reveal dual-core maxima over the ITCZ and East Asia. Discontinuous types exhibit consistent spatial patterns relative to continuous MCSs, despite intensity hierarchy (merging > complex > splitting). They enhance ITCZ rainfall by 4–16% via intensified updrafts and colder cloud tops, contrasting sharply with East Asia's precipitation suppression (–16% to 0) tied to disrupted cloud structure and reduced convective instability. The findings provide critical insights for improving flood early-warning systems and optimizing agricultural water management in monsoon-vulnerable regions, directly supporting climate adaptation strategies and sustainable development goals.

Mesoscale Convective Systems (MCSs) are primary contributors to precipitation in tropical and subtropical regions¹. The heavy rainfall events they trigger often lead to floods, profoundly impacting agriculture, water resource management, and socioeconomic activities². Globally, MCSs account for approximately 50% of total precipitation, exceeding 70% in extreme rainfall events^{3–5}. Beyond modulating atmospheric circulation through latent heat release, MCSs also influence regional energy balance via cloud-radiation feedback, making them critical components in coupled weather-climate studies⁶. Therefore, a deeper understanding of MCS evolution and associated precipitation mechanisms is vital for improving extreme weather prediction capabilities and optimizing parameterization schemes in atmospheric models⁷.

The life cycle of MCSs—spanning initiation, development, maturity, and dissipation—is closely tied to precipitation efficiency. Classical studies have established statistical relationships between MCS area, duration, and rainfall intensity using radar and satellite observations⁸. Recent advancements in high-resolution satellite data have facilitated the development of MCS tracking techniques, enabling quantitative analyses of motion vectors, cloud-top temperature evolution, and life cycle characteristics⁹. Typically, MCSs produce the heaviest rainfall at around one-third of their life cycle^{10,11}. However, existing research predominantly focuses on continuous-type

MCSs, leaving a gap in systematic exploration of discontinuous evolution processes (e.g., splitting, merging) and their dynamic-thermodynamic mechanisms.

Merging and splitting processes are critical dynamical drivers of MCS-related precipitation efficiency. Case studies revealed that merging processes generally enhance low-level convergence, prolong system longevity, and intensify rainfall^{12–14}, while splitting processes have a more variable impact, potentially suppressing convection or triggering new systems^{15,16}. Additionally, cloud–cloud interactions, such as microphysical adjustments from multi-system collisions, can significantly alter precipitation particle spectra^{17,18}. Nevertheless, current studies rely heavily on case analyses or idealized simulations, lacking statistical characterization of real-world MCS evolution types, their regional dependencies, and quantitative linkages to precipitation fields.

Despite progress in MCS evolution research, key challenges remain in systematically evaluating the precipitation contributions and physical mechanisms of discontinuous MCS types and clarifying the regulatory pathways of MCS evolution on precipitation across diverse environments. Addressing these gaps, this study employs Himawari-8 satellite data and GPM precipitation products to develop a tracking-driven classification algorithm for MCS evolution, analyzing spatiotemporal patterns of variant evolution types. Through dynamical-statistical diagnostics, we reveal

¹Key Laboratory of Tropical Atmosphere–Ocean System, School of Atmospheric Sciences, Sun Yat-Sen University, Zhuhai, China. ²Southern Marine Science and Engineering Guangdong Laboratory (Zhuhai), Zhuhai, China. ✉ e-mail: chenyulun3@mail.sysu.edu.cn

precipitation disparities in discontinuous MCSs across different regions, highlighting cross-scale interactions between environmental factors and intrinsic processes.

Results

This study classifies MCSs into four primary categories and four secondary categories. The four primary MCS evolution types, including one continuous type and three discontinuous types (merging, splitting, and complex), account for 62.14% of the total MCS population but contribute 97.15% of the total MCS-related precipitation. In contrast, the four secondary MCS types (sub-continuous, sub-merging, sub-splitting, and dissipation) constitute 37.86% of the total MCS population yet contribute only 2.85% of the total precipitation. Given the significant disparity in precipitation contributions, this study focuses on the four primary evolution types of MCSs.

We first analyze the spatial distribution characteristics of precipitation associated with four types of MCSs. Observational results reveal that the mean precipitation distributions across all four MCS types align closely with the overall precipitation field (Fig. S2 in the Supplementary File), collectively displaying a dual-core spatial structure (demarcated by dashed rectangles in Fig. 1). The primary precipitation core is anchored over the Intertropical Convergence Zone (ITCZ), while the secondary core extends along the East Asian coastal belt (Hereafter East Asia). Both regions exhibit sustained precipitation intensities exceeding 2.5 mm h^{-1} (Fig. 1a). Additional high-intensity precipitation centers ($>2.5 \text{ mm h}^{-1}$) are identified over the Bay of Bengal (BOB) and the southern Himalayan slopes. Notably, precipitation intensities in high-latitude and inland arid regions remain comparatively subdued, attributable to moisture

transport limitations and markedly reduced cloud-top heights. Nevertheless, most areas in these regions maintain baseline precipitation intensities above 0.3 mm h^{-1} .

Regarding the impact of discontinuous MCS processes on precipitation intensity, the initial theoretical hypothesis suggested that the splitting process of MCS accompanied by divergent flow fields might inhibit heavy precipitation development¹⁹, while merging processes associated with convergent fields should enhance precipitation^{14,20}. However, quantitative analysis results contradict these initial assumptions. By calculating precipitation intensity difference fields between merging, splitting, and complex MCSs relative to continuous MCSs (Fig. 1b–d), the three discontinuous MCS types show highly consistent spatial patterns in precipitation differences, varying only in magnitude. This phenomenon suggests that discontinuous MCS types may share similar dynamic–thermodynamic precipitation mechanisms.

Specifically, within the ITCZ domain (5°S – 15°N , 90°E – 180°E), the discontinuous MCSs produce 0.2 – 0.8 mm h^{-1} (around 4–16%) stronger precipitation than continuous MCSs. Conversely, the East Asian coastal sector (30°N – 45°N , 100°E – 160°E) exhibits pronounced negative anomalies (-0.8 to 0 mm h^{-1} , around -16% to 0). A moderate positive anomaly ($\sim 0.2 \text{ mm h}^{-1}$) characterizes the BOB, while the southern Himalayas persist as a precipitation stronghold dominated by continuous-type MCS activity. Besides, discontinuous MCSs display enhanced precipitation in moisture-limited environments, particularly across high-latitude zones and continental arid regions.

To rigorously assess the spatial consistency of precipitation difference fields among discontinuous MCS types, we employ statistical

Fig. 1 | Horizontal distributions of MCS-related rain rate. Average **a** rain rate produced by continuous-type MCSs and **b–d** rain rate differences between three discontinuous- and continuous-type MCSs during June–August 2016–2020. Zero-rain-rate grids are also incorporated in the statistics. The northern dashed rectangle indicates East Asia, while the southern one indicates ITCZ.

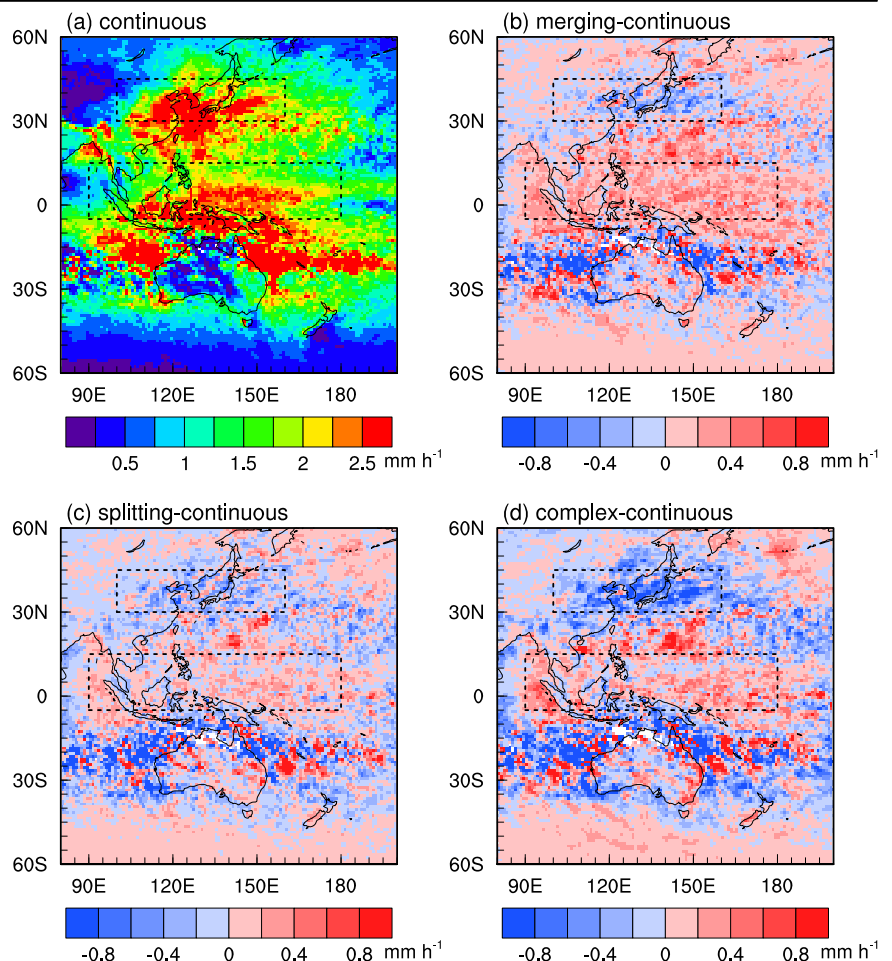
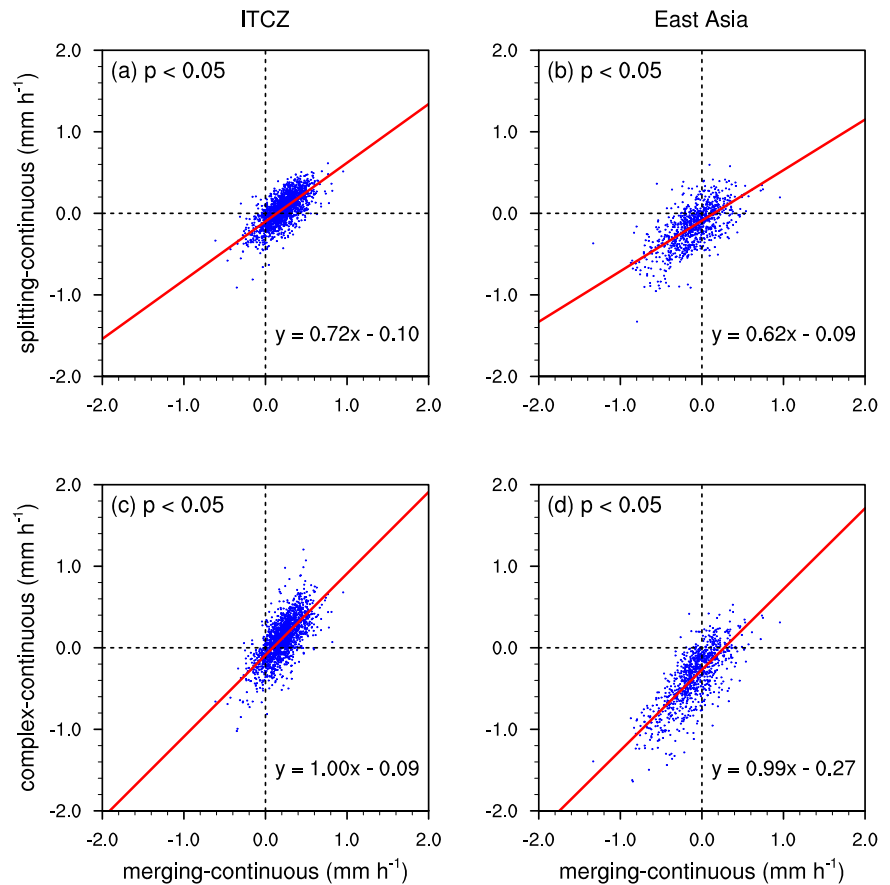


Fig. 2 | Scatter plots of average rain rate differences among discontinuous MCS types. Scatters **a, b** between merging-continuous and splitting-continuous and **c, d** between merging-continuous and complex-continuous over the ITCZ and East Asia. Each point represents a $1^\circ \times 1^\circ$ grid in the study region, with the red line indicating the linear regression fit of scatters.



correlation analysis and regression-based analytical methods. Analyses are conducted at $1^\circ \times 1^\circ$ resolution from Fig. 1b–d, incorporating only grid cells with >50 samples to ensure statistical reliability. Statistical validation demonstrates significant positive intercorrelations ($p < 0.05$) between precipitation anomaly fields of merging-, splitting-, and complex-type MCSs, mathematically verifying their shared spatial coupling patterns (Fig. 2).

In the regression analysis framework, precipitation anomalies from merging-type MCSs (calculated merging minus continuous) serve as the independent variable (x -axis). The regression equation established between rainfall anomalies of merging- and splitting-type MCSs (Fig. 2a, b) features a slope of 0.72 (0.62) and a negative intercept of -0.10 (-0.09) over ITCZ (East Asia). These parameters suggest that under equivalent geographical forcing, splitting-type MCSs demonstrate systematically reduced precipitation intensification capacity, exhibiting approximately 30% weaker enhancement compared to merging-type systems. In contrast, complex-type MCSs (Fig. 2c, d) follow the relationship $y = 0.89x - 0.09$ ($y = 0.99x - 0.27$) over ITCZ (East Asia), indicating nearly linear proportionality with merging-type anomalies. However, the negative intercept also reveals a persistent systematic deficit of 0.09 (0.27) mm h⁻¹ in precipitation intensity relative to merging-type counterparts.

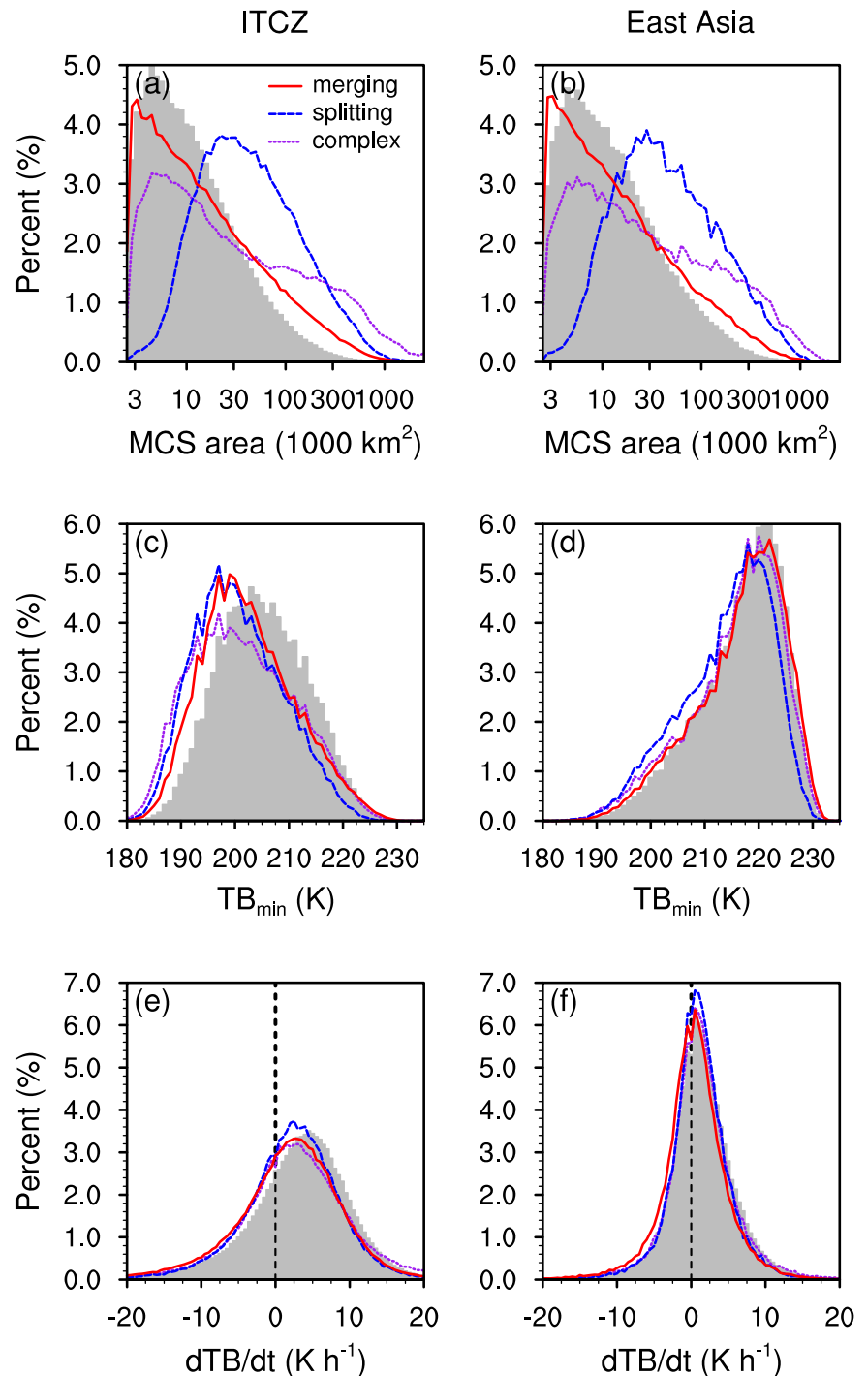
This gradient hierarchy also demonstrates the local precipitation intensity ranking: merging-type > complex-type > splitting-type. Combined with previous researches, this hierarchy may originate from (1) merging processes enhance low-level convergence through multi-cell interactions, promoting sustained updraft development; and (2) splitting processes accompanied by mid-upper-level divergent flows may prematurely consume convective available potential energy, limiting precipitation intensity.

To elucidate the intrinsic mechanisms governing precipitation differences between non-continuous and continuous MCS types, we conducted probability density function (PDF) analyses of key physical parameters of MCS across ITCZ and midlatitude East Asian coastal regions (Fig. 3), focusing on three diagnostic dimensions: horizontal scale, cloud-top thermodynamic state, and evolutionary processes.

The horizontal scale of MCS is positively related to precipitation intensity (Houze et al.⁸). Our analysis reveals analogous MCS area distributions across key regions. MCS area span three orders of magnitude (2.5×10^3 – 1.0×10^6 km²), encompassing meso- β ($< 3 \times 10^4$ km²) to meso- α ($> 3 \times 10^4$ km²) convective systems (Fig. 3a). Continuous-type MCS exhibit peak occurrence at $\sim 4.5 \times 10^3$ km², while merging-, splitting-, and complex-type MCS peak at 3.1×10^3 , 2.22×10^4 , and 4.5×10^3 km², respectively. Meso- α MCS account for 18.0%, 27.5%, 58.6%, and 43.2% of continuous, merging, splitting, and complex types. This scaling hierarchy suggests that Splitting processes predominantly occur in larger-scale MCS systems, likely associated with dissipation-phase dynamical instabilities. Complex-type MCS in favor of intermediate scales reflects enhanced cloud-process interactions in extended systems. The striking spatial similarity in scale distributions between ITCZ and East Asia precludes horizontal scale as the primary driver of precipitation disparities in the key regions.

The minimum 10.4 μ m brightness temperature of MCS (TB_{min}), a proxy for convective vigor²¹, exhibits distinct regional PDF patterns (Fig. 3c, d). The ITCZ displays dominant TB_{min} peaks at 195–200 K (deep convection), contrasting with East Asian maxima near 220 K (weaker convection) consistent with monsoonal frontal precipitation characteristics²². Notably, discontinuous MCS systematically exhibit colder cloud tops than continuous types (ITCZ: 197 K vs. 203 K; East Asia: 220 K vs. 222 K), particularly demonstrating 6 K enhancements in ITCZ convective intensity.

Fig. 3 | Probability density functions (PDFs) of key physical parameters of MCS. PDFs of **a, b** MCS area, **c, d** minimum brightness temperature ($T_{B_{min}}$), and **e, f** temporal variations of $T_{B_{min}}$ (dTB/dt) over the ITCZ and East Asia. The gray shaded areas represent continuous-type MCSs, and colored lines denote discontinuous-type MCSs.



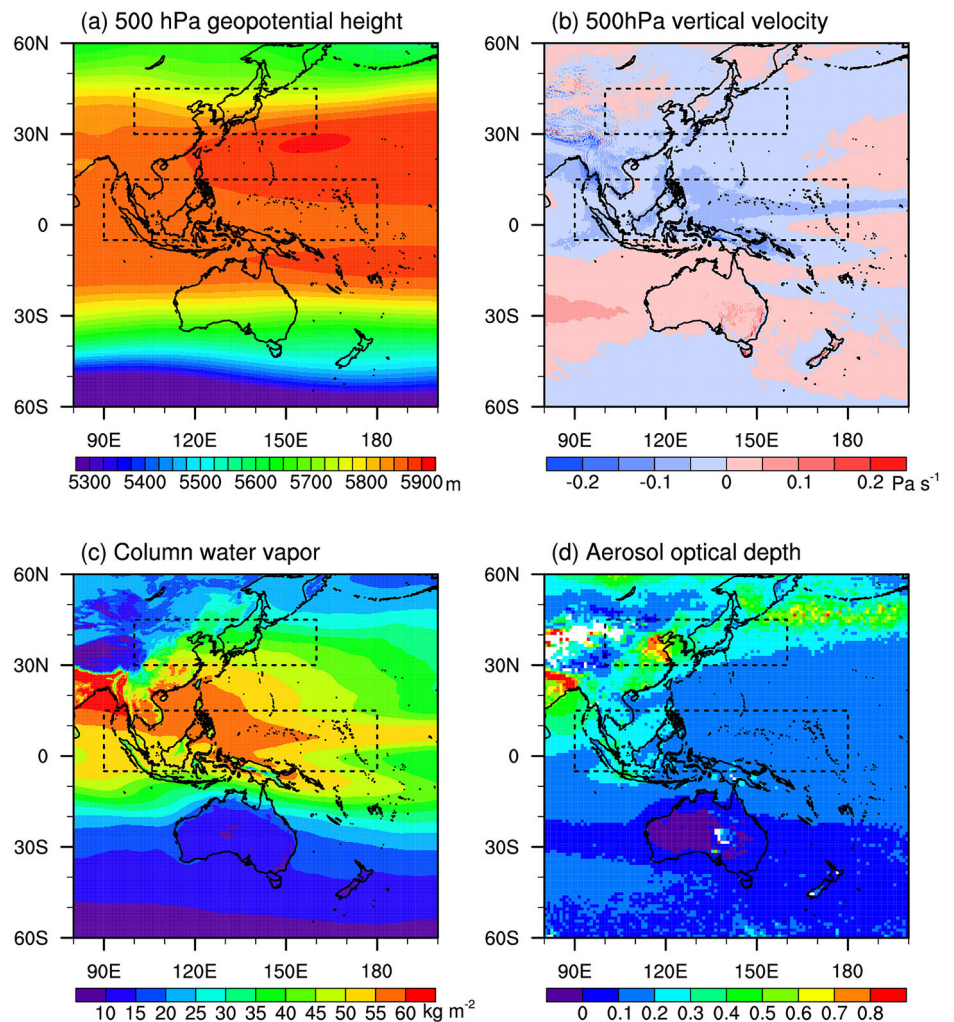
Splitting-type MCS show marginally taller tops than merging/complex types, ordered as: splitting > complex > merging > continuous.

The temporal variations of $T_{B_{min}}$, quantified by its time derivative (dTB/dt), serve as a diagnostic metric for MCS life-cycle stages¹⁰: negative dTB/dt values (cloud-top cooling) indicate the intensification stage, near-zero dTB/dt values (thermodynamic equilibrium) correspond to the mature stage, and positive dTB/dt values (cloud-top warming) mark the dissipation stage. All MCS types exhibit quasi-normal dTB/dt distributions (Fig. 3e, f), with ITCZ systems showing greater variability ($dTB/dt \in [-20, 20] \text{ K h}^{-1}$) than East Asian counterparts ($dTB/dt \in [-10, 10] \text{ K h}^{-1}$). The right-skewed dTB/dt peaks across regions reflect prolonged dissipation phases relative to intensification periods. Notably, discontinuous MCS in

the ITCZ exhibit 2 K h^{-1} stronger cooling rates than continuous types (peaks of PDFs), indicating enhanced convective triggering during discontinuous processes. Conversely, the PDFs of MCS types over East Asia show minimal inter-type divergence, suggesting regional environmental constraints dominate over intrinsic MCS variability.

The multivariate analysis of precipitation determinants, including moisture transport, dynamical forcing, and aerosol-cloud interactions, reveals key regional contrasts (Fig. 4). In the ITCZ region (Fig. 4a, c), the persistent low-level convergence driven by Hadley circulation induces deep ascent, with average vertical velocity reaching -0.07 Pa s^{-1} at 500 hPa. High column moisture levels of $50\text{--}60 \text{ kg m}^{-2}$ sustains moisture supply as well as latent heat release, while moderate aerosol conditions characterized by

Fig. 4 | Horizontal distributions of precipitation determinants. Average **a** 500 hPa geopotential height, **b** 500 hPa vertical velocity, **c** column water vapor, and **d** aerosol optical depth during boreal summer months (June–August) between 2016 and 2020.



aerosol optical depth (AOD) values of 0.1–0.3 minimize precipitation suppression.

In the East Asian region, mid-tropospheric flow is dominated by baroclinic westerlies, marked by a 500 hPa geopotential height gradient of 80 gpm per 10° latitude. The sharp meridional moisture, which declines from 50 kg m⁻² in the southern portion to 25 kg m⁻² in the northern portion, constrains northerly moisture supply in the East Asia. Heavy aerosol loading with AOD > 0.4 enhances cloud droplet competition, delaying warm rain initiation¹⁷. Weak mean ascent ($\omega = -0.03$ Pa s⁻¹ on average) disrupts the generation of deep convection.

To figure out why discontinuous processes exert opposite impacts over the ITCZ and East Asia, the thermodynamic parameters associated with different types of MCS events are further characterized (Fig. 5). In the ITCZ region, where atmospheric moisture content is exceptionally high (Fig. 4c), the development of MCSs do not rely on moisture transport by strong horizontal wind fields. The median vertical moisture flux divergence approaches zero (Fig. 5a), accompanied by relatively weak horizontal wind shear with a median value of approximately 8 m s⁻¹ (Fig. 5b). This MCSs have intense convective activity (Fig. 3c), as evidenced by a median CAPE value reaching 600 J kg⁻¹ (Fig. 5c). During discontinuous processes within MCSs, both moisture flux convergence and horizontal wind shear show moderate increases while CAPE remains essentially stable, creating favorable conditions for updraft (not shown) and precipitation enhancement.

In contrast, the East Asia region displays distinct characteristics due to its heterogeneous moisture distribution. Cloud and precipitation formation

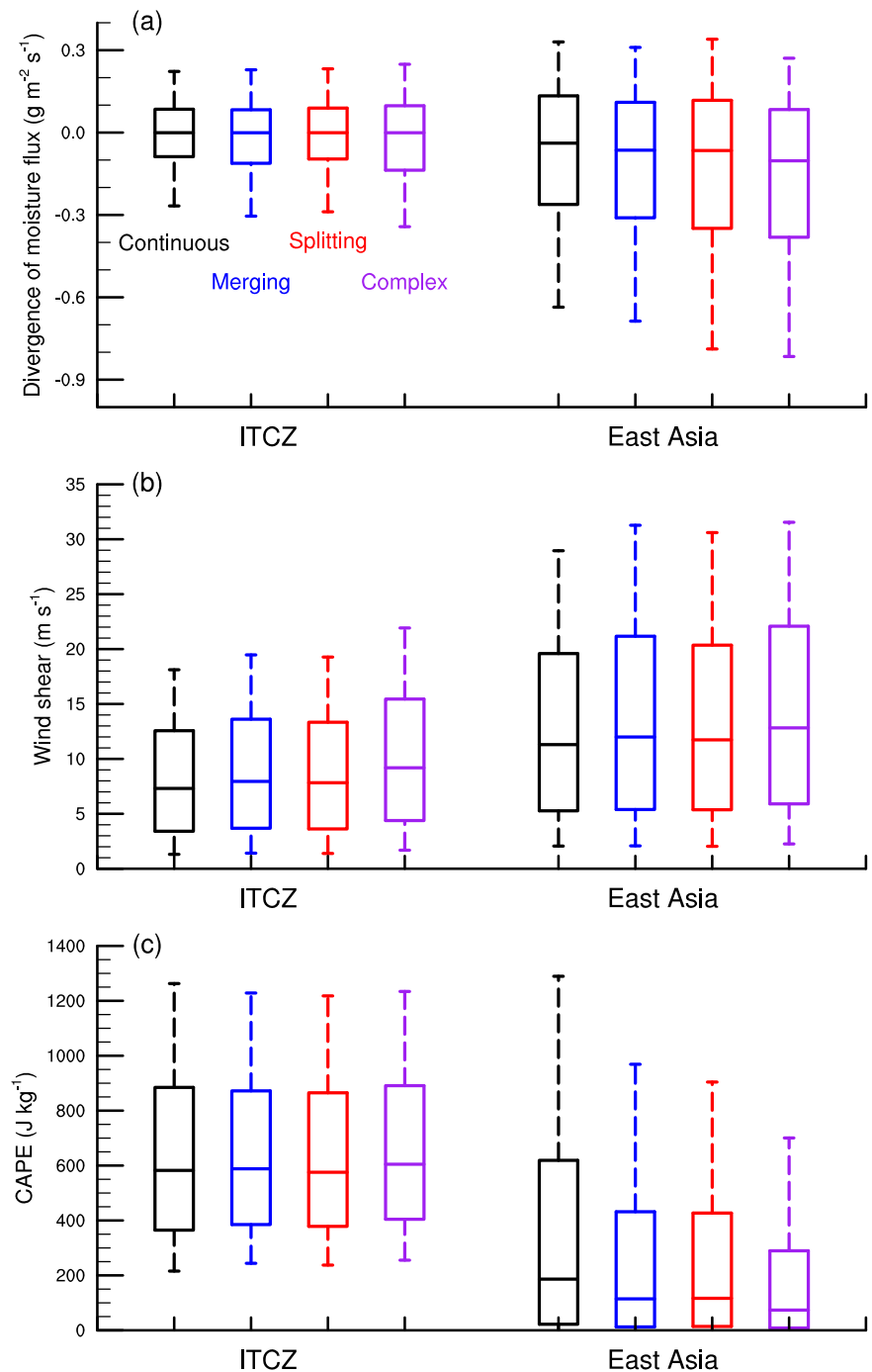
in this area critically depend on moisture transport through strong south-westerly winds (Fig. 4a, c). MCSs consequently demonstrate stronger moisture flux convergence and enhanced horizontal wind shear, with median values reaching approximately 12 m s⁻¹. Dominated by stratiform precipitation (Fig. 3d), this region shows significantly lower convective potential with a median CAPE below 200 J kg⁻¹ (Fig. 5c). During discontinuous processes within MCS, while moisture flux convergence and wind shear exhibited increases, CAPE undergoes dramatic reduction from 186 J kg⁻¹ to approximately 100 J kg⁻¹, corresponding to precipitation suppression mechanisms.

Discussion

This study elucidates the pivotal role of discontinuous MCSs in shaping regional precipitation patterns through a synthesis of satellite observations and dynamical diagnostics. The primary types of MCSs, including continuous- and discontinuous-type (merging, splitting, and complex) MCSs, despite constituting 62.14% of total MCS systems, dominate MCS-related precipitation contributions (97.15%). With a larger area than continuous MCSs, discontinuous-type MCSs exhibit even more efficient contribution. Complex-type systems exhibit 33.13% rainfall contribution, followed by merging (21.15%) and splitting types (14.53%), highlighting their critical role in extreme rainfall events.

Despite hierarchical intensity differences (merging > complex > splitting), all discontinuous MCSs exhibit spatially coherent anomaly patterns relative to continuous systems, suggesting shared thermodynamic–dynamic frameworks. In the ITCZ, discontinuous

Fig. 5 | Variations of thermodynamic parameters among different types of MCS. **a** Divergence of vertically integrated moisture flux, **b** wind shear between 200 and 850 hPa, and **c** CAPE of different types of MCSs over ITCZ and East Asia. The box plot here indicates the 90%, 75%, 50%, 25%, and 10% percentiles of the variable.



systems enhance rainfall by $0.2\text{--}0.8 \text{ mm h}^{-1}$, whereas they suppress precipitation by -0.8 to 0 mm h^{-1} in East Asia. Through systematic analysis, we further reveal distinct variations in large-scale environmental conditions, MCS characteristics, and in-cloud thermodynamical parameters between these two regions. Building on these findings, a conceptual framework (Fig. 6) that elucidates how discontinuous processes differentially modulate precipitation mechanisms across the ITCZ and East Asia is proposed:

For the ITCZ region (Fig. 6a), within deep convective precipitation regimes characterized by homogeneous high moisture availability and optimal aerosol conditions²³, discontinuous processes primarily amplify moist convective processes through intensified divergence of moisture flux and updraft though generating secondary circulations²⁴, thereby enhancing precipitation efficiency.

In the East Asian monsoon region (Fig. 6b), MCS precipitation is predominantly governed by frontal processes, where convective contributions remain limited with less than 10% of convective ratio in Meiyu frontal systems²⁵. It is suggested that discontinuous MCS processes exert precipitation suppression through disrupting the structure of stratiform clouds via strong wind shear, which subsequently reduces CAPE. Under moisture-deficient and aerosol-rich conditions (Fig. 4c, d), aerosol-mediated hydrometeor competition further suppresses warm rain formation²⁶.

Critically, while maintaining the overarching mechanistic framework, intrinsic differences emerge among the three discontinuous MCS types. Merging processes enhance precipitation through cloud-scale convergence and collision-coalescence efficiency¹². Splitting processes promote dry air entrainment and mid-level divergence, accelerating hydrometeor

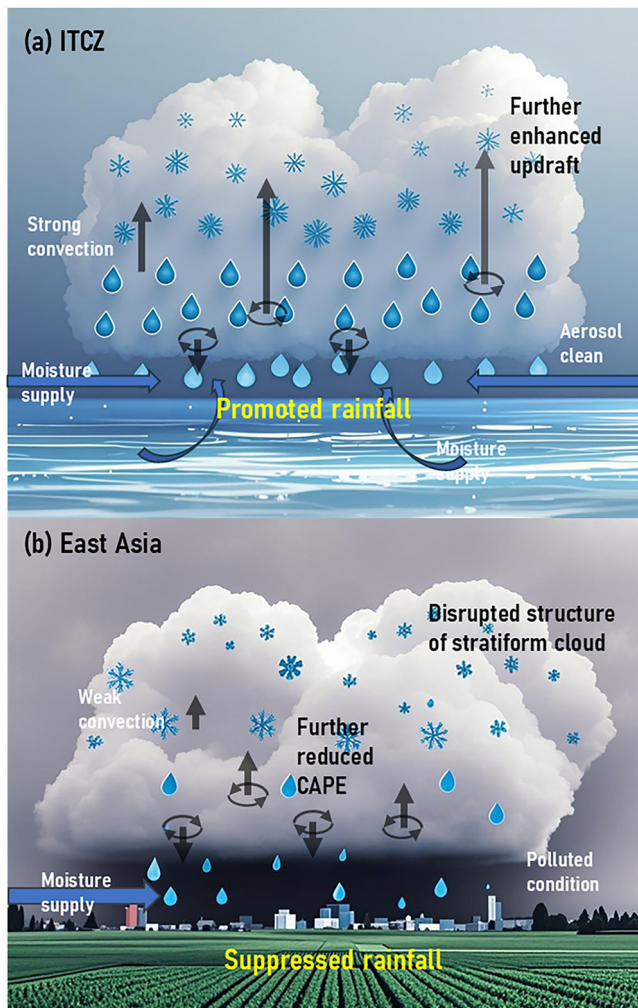


Fig. 6 | Concept of the opposite impact of discontinuous MCS evolution process. Impact of discontinuous process on precipitation intensity in **a** ITCZ and **b** East Asia. The elliptical arrows represent the secondary circulation induced by discontinuous MCS processes; the thick black arrows indicate updrafts and downdrafts; the blue arrows represent moisture transport; and the blue snowflake and raindrop symbols represent precipitation.

evaporation²⁷. Complex processes, which dynamically integrate elements of both merging and splitting processes, demonstrate intermediate precipitation impacts, with their net effects contingent on the dominance of coalescence versus evaporation pathways under specific environmental constraints.

These findings advance mechanistic understanding of MCS evolution and emphasize the necessity of incorporating cross-scale interactions between intrinsic dynamics and environmental drivers into rainfall prediction. Such improvements are critical for enhancing flood prediction accuracy in vulnerable regions like the ITCZ and East Asia, where 70% of annual flood fatalities are linked to MCS-driven extremes. Future work should integrate high-resolution simulations to unravel microphysical causality and refine parameterizations for extreme precipitation forecasting, directly addressing the World Meteorological Organization's "Early Warnings for All" initiative aimed at protecting 3 billion people from climate disasters by 2030.

Methods

Evolution categories of MCSs

We utilize Level-1B observation data from the Advanced Himawari Imager (AHI) onboard the Japan Meteorological Agency's Himawari-8 geostationary

satellite, acquired via the JAXA P-TREE system (<ftp://ftp.ptree.jaxa.jp>). Data from boreal summer months (June–August) between 2016 and 2020 are selected, with a temporal resolution of 10 min and a spatial resolution of $0.05^\circ \times 0.05^\circ$ (~ 5 km). The $10.4\text{ }\mu\text{m}$ band brightness temperature ($T_{B_{10.4}}$) data is primarily employed, as this band is less affected by atmospheric scattering effects (atmospheric transmittance $>85\%$), effectively characterizing cloud-top height and phase properties²⁸.

We identify MCS over the central coverage of Himawari-8 AHI (60°S – 60°N , 80°E – 160°W) following the classical definition by Mapes and Houze (1993) with two key criteria²⁹:

- 1) Spatial continuity: an MCS is defined as a contiguous region where adjacent grids exhibit $T_{B_{10.4}} \leq 235$ K.
- 2) Scale threshold: the effective coverage area of an MCS must be $\geq 2.5 \times 10^3 \text{ km}^2$ (~ 100 grids).

Building upon the established MCS identification criteria, we develop a tracking-driven algorithm to systematically categorize MCS evolution types. The workflow is structured as follows:

Step 1—Temporal matching. For two consecutive observation times T_0 and T_1 ($\Delta T = 30$ min, aligned with precipitation data), identify MCSs at each time step, denoted them as set $\{A_n\}$ and $\{B_n\}$, respectively.

Step 2—Motion vector estimation. Use the optical flow method to calculate the average motion vectors of $\{A_n\}$ from T_0 to T_1 , denoted as set $\{\vec{v}_n\}$. Based on these vectors, compute the theoretical positions of $\{A_n\}$ at T_1 , forming a predicted MCS set $\{A'_n\}$.

Step 3—Spatiotemporal mapping. For a specific MCS $A_1 \in \{A_n\}$, identify all elements from $\{B_n\}$ overlapping with A'_1 to form a subset $\{B'_n\}$. Subsequently, locate elements in $\{A'_n\}$ that overlap with $\{B'_n\}$, establishing the spatiotemporal mapping relationships of A_1 from T_0 to T_1 .

Step 4—Evolution type classification. Based on the mapping relationships, classify A_1 into evolution categories according to criteria outlined in Table 1. Four primary types are defined: continuous, merging, splitting, and complex, along with four secondary subtypes. Specifically, merging, splitting, and complex types are collectively termed discontinuous MCSs.

MCS-related precipitation

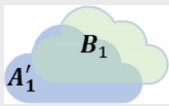
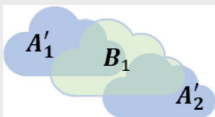
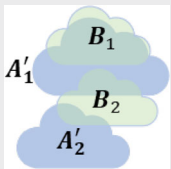
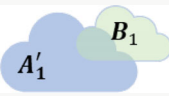
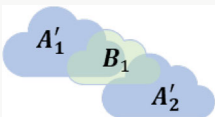
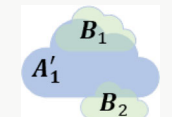
The precipitation data used in this study are derived from the GPM (Global Precipitation Measurement) gridded precipitation product, IMERG (Integrated Multi-satellite Retrievals for GPM). IMERG includes three versions: *early run*, *late run*, and *final run*, with a temporal resolution of 0.5 h and a spatial resolution of $0.05^\circ \times 0.05^\circ$ (~ 5 km). The *final run* product is selected for this analysis³⁰. Each data from IMERG *final run* has a unique start time T_0 and end time T_1 , and the given precipitation variable reflects the average rain rate between T_0 and T_1 . Therefore, IMERG data are matched to Himawari-8 AHI data near the start time T_0 to show the average rain rate during the process of cloud evolution.

For a given precipitation grid, it is classified as MCS-related precipitation if it occurs within 50 km of an MCS. If multiple MCSs fall within 50 km of the grid (a rare occurrence), the precipitation is assigned to the nearest MCS.

In this study, the four primary MCS evolution types account for 62.14% of the total MCS population but contribute 97.15% of the total MCS-related precipitation. In contrast, the four secondary MCS types (Sub-continuous, Sub-merging, Sub-splitting, and Dissipation) constitute 37.86% of the total MCS population yet contribute only 2.85% of the total precipitation. This disparity arises for two reasons. Firstly, secondary-type MCSs are typically small in scale and near dissipation, resulting in fewer occurrences in each location (see Fig. S1 in the Supplementary File). Secondly, secondary-type MCSs exhibit declining cloud-top heights and weak convective activity, leading to minimal rainfall production (see Fig. S2 in the Supplementary File).

Besides, to strengthen the analytical framework, this study additionally incorporates two supplementary datasets, including the ERA5 monthly reanalysis data with $0.25^\circ \times 0.25^\circ$ and Terra MODIS Level-3 monthly AOD products with $1^\circ \times 1^\circ$ resolution.

Table 1 | Classification criteria for the evolutionary type of MCS A_1 at time T_0

Primary types	Continuous	Merging	Splitting	Complex
Mapping	1–1	$n-1$ ($n > 1$)	$1-n$ ($n > 1$)	$n-n$ ($n > 1$)
Concept ^a				
Overlap ^b	>50%	>50%	>50%	0–100%
Proportion ^c	33.89%	14.47%	4.91%	8.87%
Rainfall contribution	28.24%	21.15%	14.53%	33.13%
Secondary types	Sub-continuous	Sub-merging	Sub-splitting	Dissipation
Mapping	1–1	$n-1$ ($n > 1$)	$1-n$ ($n > 1$)	1–0
Concept				
Overlap	≤50%	≤50%	≤50%	0%
Proportion	18.59%	5.38%	0.80%	13.08%
Rainfall contribution	1.98%	0.41%	0.15%	0.41%

^aBlue area indicates the theoretical positions of the MCS at time T_1 (predicted from T_0), while green represents the actual MCS positions observed at T_1 .

^bOverlap (ratio) refers to the proportion of the overlapping area between A'_1 and $\{B_n\}$, relative to the area of A'_1 itself.

^cProportion denotes the percentage of MCSs of this type relative to the total MCS population.

Data availability

The IMERG precipitation data was collected from the Precipitation Measurement Mission website (<https://pmm.nasa.gov>). The Himawari-8 AHI L1 gridded data was provided by the Japanese Meteorological Agency (https://www.data.jma.go.jp/mscweb/en/himawari89/space_segment/spsg_ahi.html). The ERA5 reanalysis data was collected from the ECMWF website (<https://www.ecmwf.int/>).

Received: 15 April 2025; Accepted: 10 June 2025;

Published online: 20 June 2025

References

- Angulo-Umana, P. & Kim, D. Mesoscale convective clustering enhances tropical precipitation. *Sci. Adv.* **9**, eabo5317 (2023).
- Hu, L. et al. Escalating rainstorm-induced flood risks in the Yellow River Basin, China. *Environ. Res. Lett.* **19**, 64006 (2024).
- Liu, C. & Zipser, E. J. The global distribution of largest, deepest, and most intense precipitation systems. *Geophys. Res. Lett.* **42**, 3591–3595 (2015).
- Schumacher, R. S. & Rasmussen, K. L. The formation, character and changing nature of mesoscale convective systems. *Nat. Rev. Earth Environ.* **1**, 300–314 (2020).
- Haberlie, A. M., Ashley, W. S., Gensini, V. A. & Michaelis, A. C. The ratio of mesoscale convective system precipitation to total precipitation increases in future climate change scenarios. *npj Clim. Atmos. Sci.* **6**, 150–155 (2023).
- Bouniol, D., Roca, R., Fiolleau, T. & Poan, D. E. Macrophysical, microphysical, and radiative properties of tropical mesoscale convective systems over their life cycle. *J. Clim.* **29**, 3353–3371 (2016).
- Alapaty, K. et al. Introducing subgrid-scale cloud feedbacks to radiation for regional meteorological and climate modeling. *Geophys. Res. Lett.* **39**, L24808 (2012).
- Houze, R. A. Mesoscale convective systems. *Rev. Geophys.* **42**, G4003 (2005).
- Feng, Z. et al. A global high-resolution mesoscale convective system database using satellite-derived cloud tops, surface precipitation, and tracking. *J. Geophys. Res. Atmos.* **126**, e2020JD034202 (2021).
- Fiolleau, T. & Roca, R. Composite life cycle of tropical mesoscale convective systems from geostationary and low Earth orbit satellite observations: method and sampling considerations. *Q. J. R. Meteorol. Soc.* **139**, 941–953 (2013).
- Zhang, A. & Fu, Y. Life cycle effects on the vertical structure of precipitation in East China measured by Himawari-8 and GPM DPR. *Mon. Weather Rev.* **146**, 2183–2199 (2018).
- Fu, D. & Guo, X. A cloud-resolving simulation study on the merging processes and effects of topography and environmental winds. *J. Atmos. Sci.* **69**, 1232–1249 (2012).
- Guo, X., Guo, X., Fu, D. & Fang, J. Storm splitting process and the associated mechanisms for a long-lived hailstorm. *Atmos. Res.* **281**, 106472 (2023).
- Schumacher, R. S. & Johnson, R. H. Organization and environmental properties of extreme-rain-producing mesoscale convective systems. *Mon. Weather Rev.* **133**, 961–976 (2005).
- Čurić, M., Janc, D. & Vučković, V. The influence of merging and individual storm splitting on mesoscale convective system formation. *Atmos. Res.* **93**, 21–29 (2009).
- Lagare, C., Yamazaki, T. & Ito, J. Numerical simulation of a heavy rainfall event over Mindanao, Philippines, on 03 May 2017: mesoscale convective systems under weak large-scale forcing. *Geosci. Lett.* **10**, 23 (2023).
- Rosenfeld, D. et al. Flood or drought: how do aerosols affect precipitation?. *Science* **321**, 1309–1313 (2008).
- Sheikh, M. Z. et al. Effect of turbulence on the collision rate between settling ice crystals and droplets. *J. Atmos. Sci.* **81**, 887–901 (2024).

19. Weisman, M. L. & Rotunno, R. A theory for strong long-lived squall lines" revisited. *J. Atmos. Sci.* **64**, 361–381 (2004).
20. Xu, X. et al. Dynamics of two episodes of high winds produced by an unusually long-lived quasi-linear convective system in South China. *J. Atmos. Sci.* **81**, 1449–1473 (2024).
21. Zipser, E., Cecil, D., Liu, C., Nesbitt, S. & Yorty, D. Where are the most intense thunderstorms on earth? *Bull. Am. Meteorol. Soc.* **87**, 1057–1072 (2006).
22. Day, J. A., Fung, I. & Liu, W. Changing character of rainfall in eastern China, 1951–2007. *Proc. Natl. Acad. Sci. USA* **115**, 2016–2021 (2018).
23. Schneider, T., Bischoff, T. & Haug, G. H. Migrations and dynamics of the intertropical convergence zone. *Nature* **513**, 45–53 (2014).
24. Fahrin, F., Gonzalez, A. O., Chrisler, B. & Stachnik, J. P. The relationship between convectively coupled waves and the East Pacific ITCZ. *J. Clim.* **37**, 2565–2583 (2024).
25. Zhang, A. Q. et al. Diurnal variation of Meiyu rainfall in the Yangtze plain during atypical Meiyu years. *J. Geophys. Res. Atmos.* **125**, e2019JD031742 (2020).
26. Arola, A. et al. Aerosol effects on clouds are concealed by natural cloud heterogeneity and satellite retrieval errors. *Nat. Commun.* **13**, 7357 (2022).
27. Grim, J. et al. Microphysical and thermodynamic structure and evolution of the trailing stratiform regions of mesoscale convective systems during BAMEX. Part II: Column model simulations. *Mon. Weather Rev.* **137**, 1186–1205 (2009).
28. Bessho, K. et al. An introduction to Himawari-8/9–Japan's new-generation geostationary meteorological satellites. *J. Meteorol. Soc. Jpn.* **94**, 151–183 (2016).
29. Mapes, B. E. & Houze, R. A. Cloud clusters and superclusters over the oceanic warm pool. *Mon. Weather Rev.* **121**, 1398–1415 (1993).
30. Huffman, G. J. et al. *NASA Global Precipitation Measurement (GPM) Integrated Multi-Satellite Retrievals for GPM (IMERG). Algorithm Theoretical Basis Document (ATBD) Version 4* (NASA, 2015).

Acknowledgements

This research is funded by the National Natural Science Foundation of China (Grant 42475085) and the Project supported by Southern Marine Science and Engineering Guangdong Laboratory (Zhuhai) (Grant SML2024SP013).

Author contributions

A.Z. and Y.C. discussed the central concepts and ideas and processed and analyzed data. A.Z. wrote this paper.

Competing interests

The authors declare no competing interests.

Additional information

Supplementary information The online version contains supplementary material available at

<https://doi.org/10.1038/s44304-025-00105-3>.

Correspondence and requests for materials should be addressed to Yilun Chen.

Reprints and permissions information is available at

<http://www.nature.com/reprints>

Publisher's note Springer Nature remains neutral with regard to jurisdictional claims in published maps and institutional affiliations.

Open Access This article is licensed under a Creative Commons Attribution 4.0 International License, which permits use, sharing, adaptation, distribution and reproduction in any medium or format, as long as you give appropriate credit to the original author(s) and the source, provide a link to the Creative Commons licence, and indicate if changes were made. The images or other third party material in this article are included in the article's Creative Commons licence, unless indicated otherwise in a credit line to the material. If material is not included in the article's Creative Commons licence and your intended use is not permitted by statutory regulation or exceeds the permitted use, you will need to obtain permission directly from the copyright holder. To view a copy of this licence, visit <http://creativecommons.org/licenses/by/4.0/>.

© The Author(s) 2025